IEEE Access
Multidisciplinary | Rapid Review | Open Access Journal

Received May 21, 2020, accepted June 9, 2020, date of publication June 17, 2020, date of current version June 30, 2020.

Digital Object Identifier 10.1109/ACCESS.2020.3003069

Diameter Measurement of Fuel Rods Based on Particle Swarm Optimization With All-Parameter Adaptive Mutation Mechanism

RUIRUI JI[1], PENG CHEN[1], CHENGXIANG LIU[1], LI TU[2], FULIN LIANG[1], PANSHENG GU[1], CHEN HUANG[1], AND RONG YANG[1]

[1]College of Mechatronics and Control Engineering, Shenzhen University, Shenzhen 518060, China
[2]Zhongshan Institute, University of Electronic Science and Technology of China, Zhongshan 528402, China

Corresponding author: Chengxiang Liu (chxliu@szu.edu.cn)

This work was supported in part by the National Nature Science Foundation of China under Grant 61773266 and in part by the Science and Technology Research and Development Foundation of Shenzhen under Grant JCYJ20170818144254033.

ABSTRACT In nuclear power plants, due to the special working environment, the status of the fuel rods will be changed by the influence of radiation. And these changes, such as diameter expansion, will cause damage to the fuel rods and even affect the safe operation of nuclear power plants. Therefore, it is necessary to accurate diameter measurement for nuclear fuel rods. This paper aims to solve the measurement problem of fuel rods, and proposes a measurement technique based on image processing. In the proposed scheme, based on Zhang's method, tangential distortion is considered to be an affecting factor at first to improve the accuracy of camera calibration. Then, a particle swarm algorithm with all-parameter adaptive mutation method is proposed for the optimization of camera parameters. Finally, a simple and convenient method to calculate pixel equivalent is designed by considering the feature extraction of corner coordinates of subpixel to accurately obtain pixel equivalents. The effectiveness of this measurement scheme is highlighted on a measuring platform. The relative error of the proposed method reaches 0.041%, and RMSE reaches 4.16 μm. Experimental results demonstrate that this approach is efficient for high-accuracy diameter measurement of fuel rods.

INDEX TERMS Camera calibration, diameter measurement, image processing, pixel equivalent, parameters optimization, tangential distortion.

I. INTRODUCTION

In recent years, nuclear power plants have played an increasingly important role in human production and life. However, due to the particularity of energy types, nuclear power plants have brought convenience to society, but also brought new safety issues. Nuclear fuel assemblies are operated under high-temperature and high-pressure environments for a long time. Cracks, wear, and holes will inevitably occur in the fuel rod cladding. These defects will cause radioactive substances in the fuel rod cladding to leak to the primary coolant [1]. Therefore, if the damaged fuel rods are not processed, in view of operational safety considerations, the corresponding components will not be allowed to be reused, which will directly cause asset losses and increase the subsequent spent fuel treatment costs [2]. Therefore, it is necessary to continuously measure the diameter of the fuel rod to detect the broken rod in the assembly. To date, the research used for fuel rod diameter measurement has received great attention from the academia and industry.

In fact, direct measurement of fuel rods is unrealistic due to the high radiation environment. Therefore, research scholars have conducted extensive research on the remote measurement technology of fuel rods [3], [4]. Thome *et al.* [5] proposed to use an ultrasonic testing system to inspect the water presence inside of discharged fuel rods, identify the rod location, for fuel assemblies' repair or further root-cause determination. Leuthro *et al.* [6] proposed that based on the monitoring data of specific nuclide radioactivity in the primary loop of the reactor, the time of fuel element damage can be determined, the number and type of damaged fuel rods can be estimated, and the area. Beraha [7] proposed to

The associate editor coordinating the review of this manuscript and approving it for publication was Haiyong Zheng.

estimate the radioactivity level of fission products according to the reactor power, the change of discharge flow rate or the degassing process to judge whether the fuel rod is damaged. The in-core sipping method [8] mainly relies on temperature effects to promote the escape of fission products from the damaged area, and samples are taken for radioactivity measurement to detect the presence of fission products, so as to identify the damaged fuel components.

However, the above detection methods have hysteresis and uncertainty. In comparison, image processing technology is widely used for non-contact measurement because of its unique advantages. The technology can remotely collect fuel rod images through the camera before the cladding is damaged, detect the diameter of the fuel assembly, and repair or replace the damaged assembly in time. This is a strong guarantee for improving the safety and economy of nuclear power plants.

Because camera calibration is an important part of image processing, scholars have conducted a lot of research in this field. Camera self-calibration [9], camera plane calibration [10] and Tsai's two-step calibration [11] are relatively mature. In recent years, several other camera calibration methods have emerged [12], [13]. Park *et al.* [14] proposed a distortion model defined on ideal distortion-free coordinates from the perspective of distortion coordinates, which can reduce the calculation time and maintain high accuracy. Hartley and Kang [15] proposed a completely non-iterative method based on Zhang's [10] technique to simultaneously calibrate the camera's radial distortion function and intrinsic parameters. This method is fast and not affected by the local minimum. Thirthala and Pollefeys [16] identified the right camera direct or inverse distortion model by fitting real camera distortions estimated with a non-parametric algorithm. Liu *et al.* [17] proposed an image correction method based on absolute quadratic curve. Use the cross ratio invariance and extract the feature points and feature lines of the target to obtain the intrinsic parameters of the camera, and no prior information of the camera is needed.

However, only radial distortion is considered and tangential distortion [18] is ignored in the above-mentioned methods. It appears as an offset of the image point in the tangential direction and cannot be ignored in high-precision measurement. Consequently, the influence of second-order tangential distortion is considered in this paper based on Zhang [10] calibration method, which is a method between traditional calibration and self-calibration.

Camera parameter optimization is an important step to improve the calibration accuracy. Evolutionary computing techniques (evolutionary programming [19] and genetic algorithms [20]) are driven by natural evolution. According to the rule of ''survival of the fittest'', through ''genetic'' operations (such as mutation, crossover and reproduction), operate on individual groups of coding problem solutions. Eberhart and Kennedy developed an algorithm called particle swarm optimization (PSO) by simulating social behavior [21]–[23]. It is a random search algorithm based on population and fitness developed from bionics. However, these algorithms easily converge to a local minimum and reduce the calibration accuracy. Therefore, researchers combined PSO with the mutation operation in genetic algorithm to propose mutation-based PSO [24]. In this paper, PSO with an all-parameter adaptive mutation (APAM) algorithm is used as a method to optimize camera internal parameters to improve calibration accuracy. The advantage of this method is that it is not easy to fall into the local optimal solution.

Since the pixel equivalent directly affects the accuracy of the diameter measurement result, the pixel equivalent value is calibrated by selecting regions of interest (ROIs) at different positions on the checkerboard grid, and measuring the different positions of the fuel rods to improve the measurement accuracy.

This paper aims to use image processing to remotely measure the diameter of nuclear fuel rods, and takes into account the second-order tangential distortion for camera calibration, and proposes an APAM camera parameters optimization method. Compared with existing research on similar topics, the main contributions of this paper are threefold. First, in the proposed scheme, based on Zhang's method, tangential distortion is considered to be an affecting factor to improve the accuracy of camera calibration. Then, a particle swarm optimization with all-parameter adaptive mutation algorithm is proposed for the optimization of camera parameters. The biggest advantage of this scheme is that it is not easy to fall into the local minimum during the optimization process. Finally, a simple and convenient method to calculate pixel equivalent is designed by considering the feature extraction of corner coordinates of subpixel to accurately obtain pixel equivalents.

The rest of the paper is structured as follows. The process of establishing a camera model and distortion model is described in Section II. In Section III the camera intrinsic parameters are obtained using the classical Zhang's method, and the APAM strategy is used to optimize the parameters. Section IV presents an evaluation method for distortion correction effect and a calculation method for pixel equivalents in ROIs. Evaluation and verification using standard parts are also performed. Section V discusses the experimental results of the nuclear fuel rod. Section VI elaborates the conclusions.

II. MODELING

A. CAMERA MODEL

The basis of using image processing technology for high-precision measurement is to establish a strict camera model. The camera model is the geometric mapping relationship between the three-dimensional (3D) space point and the corresponding two-dimensional coordinate point in the camera coordinate system. The pinhole imaging model established in this paper describes the geometric characteristics of the target point, the collinearity of the image point and the projection center, and its structure is shown in Figure 1. In the established model, the photosensitive sensor of the camera is

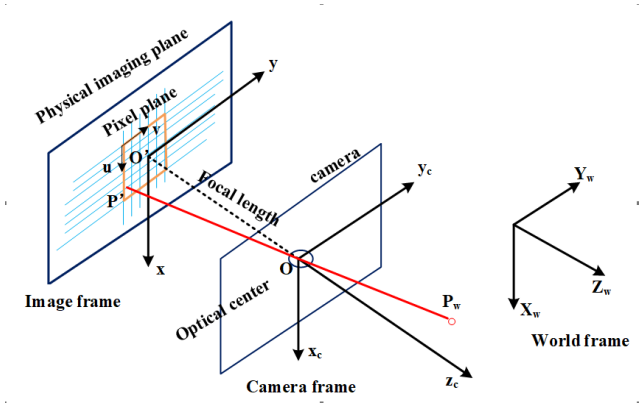

FIGURE 1. Ideal pinhole imaging model.

located near the focal point. When the approximate focus is on the plane of the photosensitive sensor, that is, the distance from the center of the convex lens to the photosensitive sensor is the focal length, the camera model at this time can be approximated as an ideal pinhole model.

The model involves four coordinate systems: a world coordinate frame (X_w, Y_w, Z_w), a camera coordinate frame (x_c, y_c, z_c), an image coordinate frame (x, y), and a pixel coordinate frame (u, v). The homography matrix describes the conversion relationship between objects in the world and pixel coordinate systems. The world coordinate system is described on the model plane of Z = 0 [16]. Thus, the following formula (1) is obtained:

$$s\begin{bmatrix} u \\ v \\ 1 \end{bmatrix} = A\begin{bmatrix} r_1 & r_2 & r_3 & t \end{bmatrix}\begin{bmatrix} X_w \\ Y_w \\ Z_w \\ 1 \end{bmatrix} \xrightarrow{Z_w=0} s\begin{bmatrix} u \\ v \\ 1 \end{bmatrix} = A\begin{bmatrix} r_1 & r_2 & t \end{bmatrix}\begin{bmatrix} X_w \\ Y_w \\ 1 \end{bmatrix}, \tag{1}$$

where the intrinsic matrix

$$A = \begin{bmatrix} f_x & \gamma & u_0 \\ 0 & f_y & v_0 \\ 0 & 0 & 1 \end{bmatrix}$$

is the camera intrinsic parameter matrix and (u_0, v_0) represent the coordinates of the principal point; f_x and f_y are the scale factors in the u and v axes of the image, and γ is a parameter describing the skew of the image axes, which is imposed as the skewless constraint 0. The extrinsic parameter $R = \begin{bmatrix} r_1 & r_2 & r_3 \end{bmatrix}$ is the rotation matrix consisting of the unit rotation vectors r_1, r_2, and r_3. $t = \begin{bmatrix} t_1 & t_2 & t_3 \end{bmatrix}^T$ is the translation vector, and s is an arbitrary scale factor.

B. DISTORTION MODEL

The ideal pinhole model will ignore the deformation of the camera and will inaccurately describe the geometric relationship of the imaging, resulting in the problem of skew in imaging. This problem is mainly caused by radial and tangential distortions when the camera collects images. However, in Zhang's method, only the radial distortion of the image is thoroughly researched and compensated, but the influence of tangential distortion on imaging is not involved. Therefore, this paper considers the second-order radial and tangential distortion based on Zhang's calibration method, and establishes the corresponding mathematical model.

1) RADIAL DISTORTION

Radial distortion causes an inward or outward displacement of a given image point from its ideal location. This type of distortion is mainly caused by flawed radial curvature curve of the lens elements.

The radial distortion of a perfectly centered lens is governed by expression of the following form [25], [26]:

$$\begin{aligned} x_{RLD} &= x_d(k_1 r^2 + k_2 r^2) \\ y_{RLD} &= y_d\left(k_1 r^2 + k_2 r^4\right) \\ r^2 &= x_d^2 + y_d^2, \end{aligned} \tag{2}$$

where r is the radial distance from the principal point of the image plane, and (x_d, y_d) is the distorted coordinate. k_1, k_2, are the first-order and second-order coefficients of radial distortion, respectively.

2) DECENTERING DISTORTION

Actual optical systems are subject to various degrees of decentering, that is, the optical centers of lens elements are not strictly collinear. This defect introduces what is called decentering distortion. This distortion has both radial and tangential components, which can be described analytically by the following expressions [27]:

$$\begin{aligned} x_{DLD} &= p_1\left(3x_d^2 + y_d^2\right) + 2p_2 x_d y_d \\ y_{DLD} &= p_2\left(3y_d^2 + x_d^2\right) + 2p_1 x_d y_d, \end{aligned} \tag{3}$$

where p_1 and p_2 are second-order radial tangential distortion coefficients.

Therefore, the total distortion has both radial and tangential components, which can be described analytically by the following expressions [28], [29]:

$$\begin{aligned} x_u &= x_d + x_d\left(k_1 r^2 + k_2 r^4\right) + p_1\left(3x_d^2 + y_d^2\right) + 2p_2 x_d y_d \\ y_u &= y_d + y_d\left(k_1 r^2 + k_2 r^4\right) + p_2\left(3y_d^2 + x_d^2\right) + 2p_1 x_d y_d \\ r^2 &= x_d^2 + y_d^2, \end{aligned} \tag{4}$$

where (x_u, y_u) is the undistorted coordinate.

III. CALIBRATION AND OPTIMIZATION METHOD

A. CAMERA CALIBRATION

Camera calibration is an important part of obtaining distortion parameters and performing distortion compensation. The quality of the calibration results will directly affect the measurement accuracy. In this paper, 22 plane checkerboard patterns with known side lengths were collected at

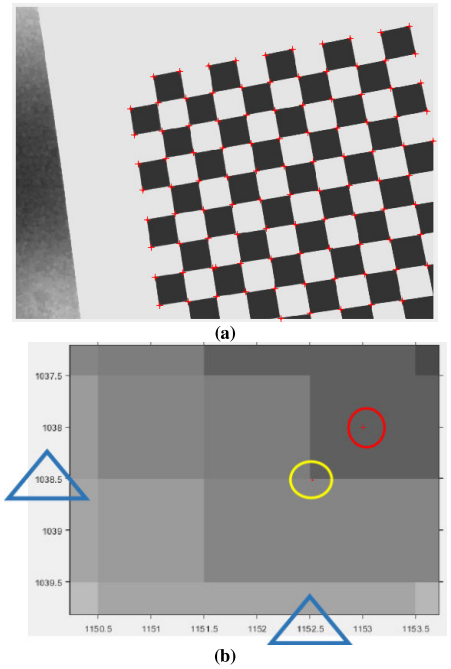

FIGURE 2. Corner extraction. (a) Harris operator for corner extraction. (b) Subpixel-level corner extraction, red circle: the corner point of the pixel level; yellow circle: corner points of subpixel level; subpixel precision to 0.1 pixels.

TABLE 1. Intrinsic initial value.

Parameters	Value
$[f_x \quad f_y]$	[2386.33664 2386.33664]
$[u_0 \quad v_0]$	[421.00000 300.00000]
γ	0.00000
$[k_1 \quad k_2 \quad p_1 \quad p_2]$	[0.00000 0.00000 0.00000 0.00000]

first. Preprocess the checkerboard image through gray-scale image transformation, smoothing and denoising. The edges of the processed image are sharpened, which is beneficial for the subsequent feature extraction of corner points. Secondly, the Harris operator [30] is used to extract the features of the checkerboard image, and the quadratic surface fitting method is used to approximate the corner response function for subpixel corner extraction, as shown in Figure 2. The point in the red circle in Fig. (2b) is the sub-pixel corner points. Finally, the intrinsic matrix is obtained by least squares, and the initial parameter values of the camera are obtained. The results of the calibration are shown in Table 1.

B. OPTIMIZATION ALGORITHM

The above internal parameters are obtained under the ideal state without distortion. However, distortion is not negligible in practical applications. Therefore, it is necessary to combine the above solution with a distortion model to obtain distortion parameters and achieve the purpose of improving the camera calibration accuracy. This is the process of parameter optimization.

TABLE 2. Results of MLE optimization.

Parameters	Value
$[f_x \quad f_y]$	[2350.17737 2352.62933]
$[u_0 \quad v_0]$	[390.49817 296.24678]
γ	0.00000
$[k_1 \quad k_2 \quad p_1 \quad p_2]$	[–0.11884 1.77822 0.00015 –0.00358]

1) MLE

The parameter optimization method used in Zhang's calibration method is MLE. This paper implements it as one of the parameter optimization methods and compares it with the proposed method. MLE is an important method for obtaining estimates, and its goal is to find a phylogenetic tree with a higher probability of generating observation data. It is one of the most important, most widely used, and most effective parameter estimation methods in statistics, and can theoretically obtain the best performance. It can also be used as a nonlinear optimization algorithm and a nonlinear parameter learning algorithm, which can quickly and accurately converge [31]. Using the MLE method requires that the image is disturbed by Gaussian noise. The size of the noise is the error caused by the observation under the assumption that the density function of the Gaussian noise is known. About MLE, please refer to references [32]–[34].

From the perspective of estimation, MLE makes effective use of the information provided by each observation. It uses the occurrence of the event as the most likely event as the starting point, and finds the maximum probability to obtain the estimated value of the parameter. To obtain the optimal estimation of the parameters, the following function needs to be minimized [10]. This is a nonlinear minimization problem, which can be solved as implemented in Minpack [35], using the LM algorithm to obtain MLE:

$$\sum_{i=1}^{n}\sum_{j=1}^{m}\left\|m_{ij}-\hat{m}(A,R_i,t_i,M_j)\right\|^2, \tag{5}$$

where n and m are the numbers of checkerboard images and corners, respectively. m_{ij} is the extracted corner pixel coordinates, and $\hat{m}(A, R_i, t_i, M_j)$ is the projection of the point M_j in the image i.

The refine results are shown in Table 2. However, LM algorithm is usually lost in a local minimum and reduces the calibration accuracy.

2) PROPOSED PSO WITH APAM

The significant advantage of PSO algorithm over MLE is that it does not depend on the analytical nature of the objective function.

PSO is a random search scheme suitable for nonlinear optimization and an iterative algorithm based on population and fitness. By determining the fitness function, the global and local extremums are searched in parallel to find their numerical solution. The parameter setting of PSO is simple, but there are shortcomings such as premature convergence and easy to fall into the local optimal solution.

Therefore, this paper proposes the PSO algorithm with APAM. The improved algorithm introduces the concept of average particle distance, while adding adaptive inertia factor, adaptive mutation rate, adaptive local learning factor and adaptive global learning factor, enriching the population Diversity improves the local and global search capabilities of particles, which can effectively avoid the local optimal value of particles and approach the global optimal value.

The fitness function $Q(\xi)$ is defined in the practical problem of optimizing the intrinsic parameters. This function defines the pixel coordinates abstracted by the corners and the two norms of the re-projection points, that is, the distance between the two coordinate points. The minimum value is guaranteed to obtain the target solution, that is,

$$\arg\min_{\xi} Q(\xi) = \sum_{i=1}^{n}\sum_{j=1}^{m} \left\| p_{ij} - p(\xi, R_i, t_i, P) \right\|^2, \quad (6)$$

where p_{ij} is the pixel corner coordinate and $p(\xi, R_i, t_i, P)$ is the coordinate point of the re-projection of the corners. And P is the corner coordinate of the 3D world coordinate system.

Due to the lack of population diversity, PSO exists premature convergence problems, so the concept of average particle distance $D(t)$ [24] of the population is introduced. It is used to describe the diversity of the population. The larger the $D(t)$, the greater the degree of scattering of particles in the population. $D(t)$ is shown as (7).

$$D(t) = \frac{1}{SL}\sum_{i=1}^{S}\sqrt{\sum_{j=1}^{g}\left(\xi_{ij}(t) - \bar{\xi}_j\right)}, \quad (7)$$

where S is the size of the population, L is the maximum length of the diagonal of the search space, and g represents the dimension of the particle. ξ_{ij} denotes the jth-dimensional coordinate value of the ith particle in the tth generation. $\bar{\xi}_j$ means the average of the j-dimensional coordinates of all particles in the tth generation.

Based on the initial values, randomly generated S particles of different positions and different velocities are defined as (8).

$$\xi = \begin{bmatrix} f_x & f_y & u_0 & v_0 & \gamma & k_1 & k_2 & p_1 & p_2 \end{bmatrix}, \quad (8)$$

The formula for specifying the maximum optimization velocity ($v_{\max}$) of the particles in this study is shown as (9).

$$v_{\max} = a^* (\zeta_{\max} - \zeta_{\min}), \quad (9)$$

where $a \in [0.01, 0.07]$. $\zeta_{\max}$ and $\zeta_{\min}$ are the maximum and minimum values of the search spaces of the particles in each dimension, respectively.

On the basis of the average particle distance $D(t)$ of the population, the arithmetic adjusts the adaptive inertia weight (w) and the mutation rate (δ) in line with the search ability of the particle swarm. Moreover, the adjustment rules of local and global learning factors c_1 and c_2 are premeditated, and the global optimal position is acquired to reach the optimal solution. w and δ are shown as (10) and (11).

$$w = \begin{cases} w_1 + 0.4r & \eta \geq 0.05 \\ w_2 + 0.4r & \eta < 0.05, \end{cases} \quad r \in [0, 1], \quad (10)$$

$$\delta = (\delta_{\max} - \delta_{\min})(D(t) - 1)^2 + \delta_{\min}, \quad (11)$$

where

$$\eta = \frac{|f(t) - f(t-5)|}{|f(t-5)|}$$

η represents the relative change rate of the global optimal fitness value of the population in the last fifth generation and $f(t)$ is the tth global optimal fitness value of the population. w_1 and w_2 are the set inertia weight factors. $\delta_{\max}$ and $\delta_{\min}$ are the maximum and minimum mutation rates, respectively.

All the particles in the population are sorted according to the fitness value from large to small, and h particles with the best fitness value are selected to generate h random numbers $r_i (i = 1, 2, \ldots, h)$ uniformly distributed in [0, 1]. If r_i is smaller than the currently calculated mutation rate, then the corresponding particle variation produces a new position. The formula is shown as (12).

$$\xi_{ij}^{t+1} = \xi_{ij}^{t}\left(1 + 0.5^* randn()\right), \quad (12)$$

where ξ_{ij}^{t} is the position of the jth dimension of the ith particle at the tth generation and ξ_{ij}^{t+1} is the position of the jth dimension of the ith particle at the $(t+1)$th generation. $randn()$ is a random variable subject to the Gauss(0,1) distribution which is expressed are zero mean unit variance normal distribution.

The learning factors c_1 and c_2 are expressed as (13) and (14).

$$c_1 = \begin{cases} c_1^{\min} & \varphi_1(t) < \bar{\varphi}_1 \\ c_1^{\max} & \varphi_1(t) \geq \bar{\varphi}_1. \end{cases} \quad (13)$$

$$c_2 = \begin{cases} c_2^{\min} & \varphi_2(t) < \bar{\varphi}_2 \\ c_2^{\max} & \varphi_2(t) \geq \bar{\varphi}_2, \end{cases} \quad (14)$$

where

$$\varphi_1(t) = \frac{\|p_i(t) - \xi_i(t)\|}{L}$$

$$\varphi_2(t) = \frac{\|g(t) - \xi_i(t)\|}{L}$$

$\bar{\varphi}_1$ and $\bar{\varphi}_2$ are set to 0.01 and 0.04, respectively. $\varphi_1(t)$ and $\varphi_2(t)$ are the distances between the current particle and its individual and global optimal values, and $p_i(t)$ is the optimal position of the ith particle individual. $g(t)$ represents the global optimal position, and $\xi_i(t)$ is the current position of the ith particle.

At each iteration, the velocity (v) and position (x) particles in the swarm will be updated to the previous best position

TABLE 3. The parameters setting of APAM algorithm.

Parameters	S	L	a	$c_1^{\min}$	$c_1^{\max}$	$c_2^{\min}$	$c_2^{\max}$
Values	100	200	0.03	0.6	1.2	1.8	3.5
Parameters	w_1	w_2	$\delta_{\min}$	$\delta_{\max}$	$\zeta_{\min}$	$\zeta_{\max}$	—
Values	0.6	0.2	0.01	0.1	0.8	50	—

(*pbest*) and global best position (*gbest*) [36]. The update function is given by

$$v_i(t+1) = w * v_i(t) + c_1 * rand() * (pbest_i(t) - x_i(t)) + c_2 * rand() * (gbest_i(t) - x_i(t)), \quad (15)$$

$$x_i = x_i + v_i, \quad (16)$$

where *rand*() is the random function in the range [0, 1]. Equation (15) is used to calculate the new velocity of the particle depending on its previous velocity and the distance of its current position from its own best experience (position) and the best experience of the group. The particle flies toward a new position following Equation (16). The performance of each particle is measured using a predefined fitness function, which is related to the problem to be solved.

The minimum particle distance $D_{\min} = 0.01$, which is the minimum limit threshold of $D(t)$. It is the basis for judging whether the particles are mutated. And η as a value to measure whether the population's global optimal adaptation value has changed significantly, set $\eta = 0.05$. The maximum number of iterations is set to 500 times in this paper.

The parameters of the algorithm are set as follows in Table 3:

The specific steps and purpose are as follows:

Step1: Initialization.

Step2: Calculate the $Q(\xi)$ and $D(t)$ of the particle. If the $Q(\xi)$ of the current particle is better than the individual optimal value, the $Q(\xi)$ and position of the individual optimal value are updated to the current particle's. Otherwise it remains unchanged. Then take the smallest individual optimal value from the population and compare it with the global optimal value. If the former is better than the latter, the latter's $Q(\xi)$ and its position are updated by the former's.

Step3: If $D(t) < D_{\min}$, then perform the following mutation operations:

i) Update the adaptive mutation rate δ, which changes with the transformation of $D(t)$.

ii) Sort all the particles in the population according to $Q(\xi)$ from large to small, and take the first $y(y = 40)$ particles corresponding to the random number r_i uniformly distributed in [0, 1].

iii) If $r_i < \delta$, the corresponding particle mutates and generates a new position ξ_{ij}^{t+1}.

If $D(t) > D_{\min}$, go to step 5, otherwise continue to step4.

TABLE 4. Search space of APAM.

Parameters	Search space
$[f_x \quad f_y]$	$[2386.33664 \quad 2386.33664] \pm [50 \quad 50]$
$[u_0 \quad v_0]$	$[421.00000 \quad 300.00000] \pm [50 \quad 50]$
γ	0.00000 ± 0.8
$[k_1 \quad k_2 \quad p_1 \quad p_2]$	$[0.00000 \quad 0.00000 \quad 0.00000 \quad 0.00000] \pm [0.8 \quad 0.8 \quad 0.8 \quad 0.8]$

TABLE 5. Results of APAM optimization.

Parameters	Value
$[f_x \quad f_y]$	$[2349.85382 \quad 2352.27367]$
$[u_0 \quad v_0]$	$[393.98977 \quad 296.71666]$
γ	0.00000
$[k_1 \quad k_2 \quad p_1 \quad p_2]$	$[-0.09126 \quad -0.18335 \quad 0.00003 \quad -0.00324]$

TABLE 6. Assessment of calibration.

Algorithm	Re-projection error (Pixel)
MLE	0.090000
APAM	0.080595

Step4: Recalculate the $Q(\xi)$ of each particle, and update the $Q(\xi)$ and position of the individual optimal and global optimal of the particle.

Step5: Determine whether the global optimal value of the particles changes significantly within the number of iterations. If $\eta < 0.05$, go back to step3 for mutation operation, and then continue to execute step6. Otherwise, proceed directly to step7.

Step6: Recalculate the $Q(\xi)$ of each particle, and update the $Q(\xi)$ and position of the individual optimal and global optimal of the particle.

Step7: The adaptive inertial weight w, local and global learning factors c_1 and c_2 are updated. Then update the particle velocity (v) and position (x).

Step8: Increase the number of iterations by 1. If the maximum number of iterations (500 times) is not reached, return to step2. Otherwise the iterative process ends.

According to the initial values of internal parameters in Table 1, the search space for defining the algorithm is shown in Table 4. The optimal solution is found through APAM in this search space.

The parameters are optimized by the above-mentioned equations. The flowchart of the approach is shown in Fig. 3, and the results are shown in Table 5.

The re-projection errors of the two optimization methods are given in Table 6. And it shows that the APAM algorithm is superior to the MLE algorithm in terms of optimizing camera intrinsic parameters.

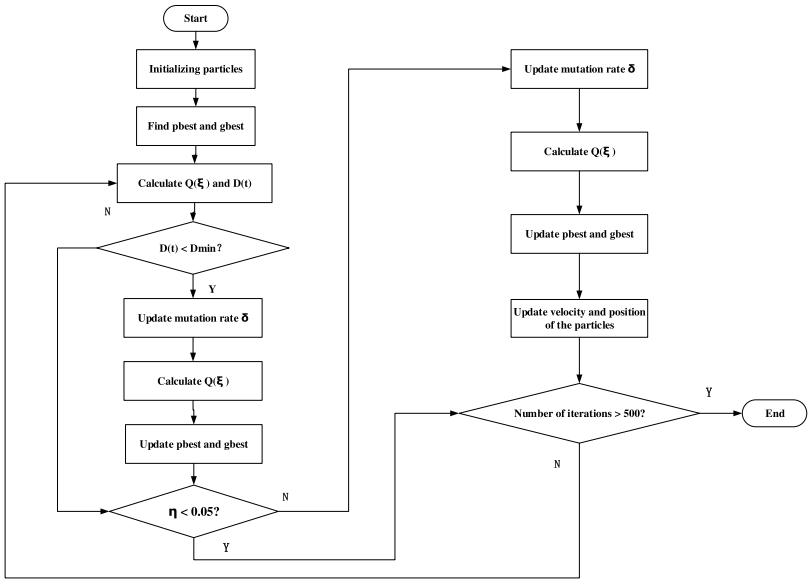

FIGURE 3. Flowchart of APAM.

IV. CORRECTION EVALUATION

In general, when evaluating the quality of a method, the simplest and most intuitive way is to perform error analysis on the experimental results. The general method of measurement analyzes the measurement error at a position where the distortion is small (e.g., the center position). However, in some momentous occasions, the changes in diameter of the fuel rods used in nuclear power plants needs to be kept in focus during operation. It is not enough to measure only the position where the distortion is small. The changes in its edge position should also be considered so as to ensure the safety of the work. Therefore, this paper designs an evaluation technique to evaluate the accuracy and reliability of the above calibration process. In this technique, based on the conventional evaluation method, and considering the difference in the degree of distortion between the edge and the intermediate position of the image, the method adds measurement error in detecting the position with large distortion (such as near the edge). And the advantages of the correction method can be evaluated according to the correction effect of the image (some or specific) position. This paper also uses standard parts of 2 mm grid and 10 mm checkerboard to verify the measurement accuracy and evaluate.

The distortion after imaging is nearly invisible to the naked eye because of the improved performance of the camera. Consequently, this paper also compares the measurement errors before and after image correction. The results further certify the necessity of distortion correction and verify the effect of the correction method.

A. CALCULATION STEPS

The key to obtain the known length of standard parts is to determine the corresponding relationship between the pixels and the actual length unit (mm/pixel), that is, the pixel equivalent [37]. An accurate pixel equivalent corresponds to precise measurement results and small errors. In theory, any object can be used as a calibrator for pixel equivalent calibration. However, in practical applications, flat objects with regular shapes are usually used as calibrators, because such calibrators facilitate image processing to calculate pixel distances.

1) FEATURE EXTRACTION

The most common method to obtain the pixel equivalent is to extract the feature points of the calibration board to obtain the pixel value, thereby calculating the ratio of the pixel value to the actual value. The feature extraction of the checkerboard is usually to retrieve its corner coordinates. Shi and Tomasi [38] subpixel corner detection method is adopted to distill the coordinates of its subpixel corner. It is improved on the basis of Harris algorithm. Define $R = \min(\lambda_1, \lambda_2)$ as the smaller of the two characteristic values. If R is greater than a predetermined threshold $\lambda_{\min}$, the point is determined to be a strong corner. The red points in Fig. 4 are the corner point coordinates of the extracted subpixel.

2) ROI SELECTION

When calculating the pixel size, we select a part of the area on the board as the ROI to locate the exact position of the corners. In this way, we can select any ROIs we want. The yellow boxes in Figure 4 are the ROIs selected in this paper. Four groups of sub-pixel distances are selected in this area. In order to reduce the final calculation error, the average value is needed calculate to obtain the pixel equivalent value.

B. EVALUATION PATTERN

In this paper, before and after the calibration of the standard parts, it is necessary to select the same area on the calibrator

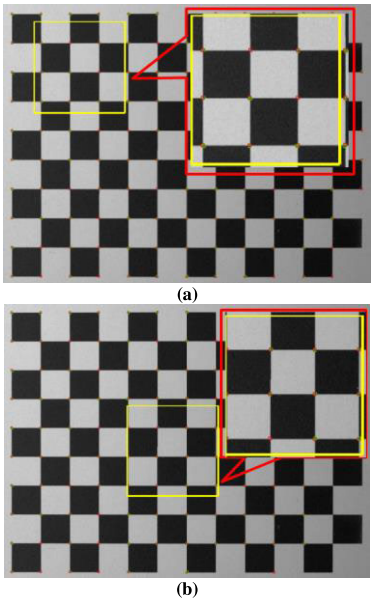

FIGURE 4. Planar checkerboard image. (a) ROI at the edge position. (b) ROI in the middle position.

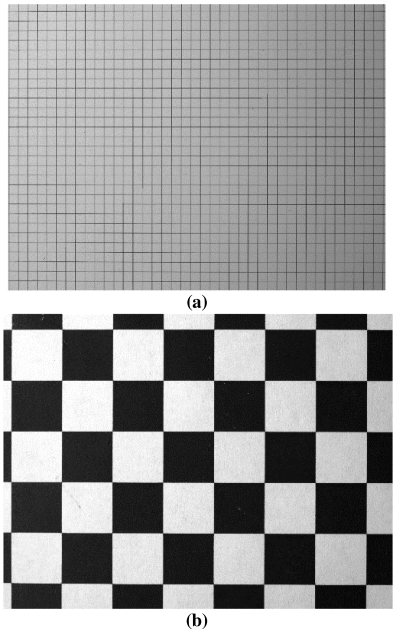

FIGURE 5. Measurement target. (a) 2 mm grid. (b) 10 mm checkerboard.

to calculate the pixel equivalent to measure the size of the standard parts. By comparing the measurement error values of the two to illustrate the necessity of correction. A repetition of the aforementioned work in conjunction with two different optimization strategies described in Section III. When in the same ROI, compare the measurement errors of different optimization methods, and evaluate the effectiveness of different methods to correct different positions. In this way, an appropriate correction method for different locations can be selected. The proposed evaluation pattern serves this purpose.

C. EVALUATION PROCESS

Two standard parts with 2 mm grid and 10 mm checkerboard are used to verify the accuracy of the above-mentioned methods.

A 5 mm calibration checkerboard and Hikvision MV-CE120-10GC industrial camera are used in this paper. The parameters obtained by OpenCV are read into the MFC program of VC++6.0 to perform corresponding correction and calculate pixel equivalents. The following sets of experiments are performed to verify the accuracy of the proposed method. The standard parts are shown in Figure 5. The resolution of the images used in the experiment is 1180×852 pixels/inch.

1) BEFORE DISTORTION CORRECTION

1. The aforementioned experiments are performed separately without any treatment on the imaged object.

1) The pixel equivalent is 0.078144 mm/pixel when the ROI is at the edge position. Fig. 6 shows the resulting graph after measurement. The magnified portion is the measured pixel distance and the calculated actual size.

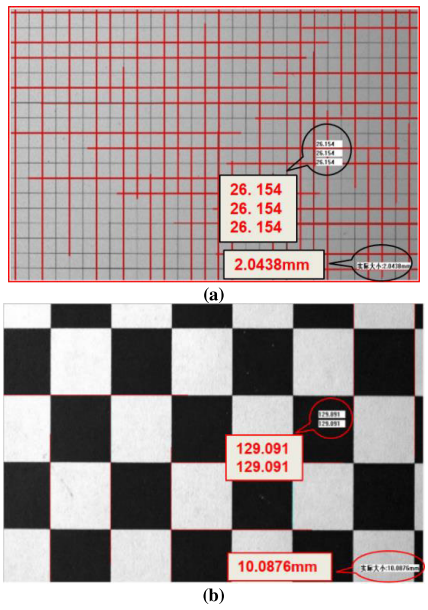

FIGURE 6. Measurement results. (a) 2 mm grid. (b) 10 mm checkerboard.

The circled data are the obtained experimental results. The upper data are the measured pixel distance, and the lower data are the calculated actual size in the figures.

2) The pixel equivalent is 0.077891 mm/pixel when the ROI is in the middle position. The same operation is performed on the two pictures. The aforementioned results and the measurement errors are shown in Tables 7 and 8.

The tables show that, if the original images without any processing are measured, then the measurement errors are large at both positions. And it is also the reason for distortion correction.

TABLE 7. Measurement results when ROI is at the edge position.

Objects	Measured value (mm)	RMSE (μm)	Relative error (%)
2 mm grid	2.0438	42.89	2.19
10 mm board	10.0876	87.25	0.876

TABLE 8. Measurement results when ROI is in the middle position.

Objects	Measured value (mm)	RMSE (μm)	Relative error (%)
2 mm grid	2.0371	36.89	1.855
10 mm board	10.0550	55.13	0.55

TABLE 9. Measurement results when ROI is at the edge position.

Objects	Measured value (mm)	RMSE (μm)	Relative error (%)
2 mm grid	2.0187	17.91	0.935
10 mm board	10.0284	28.35	0.284

TABLE 10. Measurement results when ROI is in the middle position.

Objects	Measured value (mm)	RMSE (μm)	Relative error (%)
2 mm grid	2.0122	11.79	0.61
10 mm board	9.9842	15.91	0.158

TABLE 11. Measurement results when ROI is at the edge position.

Objects	Measured value (mm)	RMSE (μm)	Relative error (%)
2 mm grid	1.9861	13.97	0.695
10 mm board	10.0131	12.92	0.131

2. The initial parameters obtained by Zhang's method are used to handle images. The experimental procedure is similar to the above-mentioned process. The results are shown in the tables below.

1) The pixel equivalent is 0.078144 mm/pixel when the ROI is at the edge position.

2) The pixel equivalent is 0.077891 mm/pixel when the ROI is in the middle position.

The aforementioned experimental data show that the results are significantly improved after the initial intrinsic parameters are provided.

2) AFTER DISTORTION CORRECTION

The parameters obtained by the two optimization methods mentioned in Section III are used to correct the distortion of the image object.

a: MLE STRATEGY

1) The pixel equivalent is 0.078024 mm/pixel when the ROI is at the near edge position.

TABLE 12. Measurement results when ROI is in the middle position.

Objects	Measured value (mm)	RMSE (μm)	Relative error (%)
2 mm grid	2.0091	9.16	0.455
10 mm board	10.0137	13.82	0.137

TABLE 13. Measuremenr results when ROI is at the edge position.

Objects	Measured value (mm)	RMSE (μm)	Relative error (%)
2 mm grid	2.0068	6.88	0.34
10 mm board	10.0035	3.62	0.035

TABLE 14. Measurement results when ROI is in the middle position.

Objects	Measured value (mm)	RMSE (μm)	Relative error (%)
2 mm grid	1.9965	3.49	0.175
10 mm board	9.9963	3.68	0.037

2) The pixel equivalent is 0.077625 mm/pixel when the ROI is in the middle position.

The relative error of the objects is significantly decreased with the MLE optimization compared with before correction. Tables 11 and 12 indicate that the relative errors of small-sized objects are still the largest compared with the others. The results of 10 mm board at different locations in two groups indicate that the distortion correction effect is good.

b: APAM STRATEGY

1) The pixel equivalent is 0.078041 mm/pixel when the ROI is at the edge position.

2) The pixel equivalent is 0.077641 mm/pixel when the ROI is in the middle position.

The corresponding measurement results are shown in Tables 13 and 14.

Generally speaking, no matter where the ROI is selected, the lens distortion correction effect of APAM is the best, especially for the chessboard. Tables 13 and 14 show that the relative error obtained using the APAM strategy is 0.035% at the edge position and 0.037% at the middle position. Both meet the requirement that the measurement error is within 10 μm.

The above experimental data shows that even if the distortion of the CCD image is invisible to the naked eye, it cannot be ignored from the perspective of measurement. The relatively large measurement error of small detection objects is the common point of the above experimental results. And the correction effect of the middle position is better than the edge. Hence, for high-precision measurement, no matter where ROI (edge or middle) is selected, the results of the APAM strategy can meet the requirements. Therefore, when it is necessary to measure different positions of the object,

TABLE 15. Repeatability of fuel ROD diameter measurement.

Type	Measured value (mm)		Measured error			
	Measured positions		RMSE (μm)		Relative error (%)	
	Edge	Middle	Edge	Middle	Edge	Middle
Without treatment	9.4374	9.4582	63.13	42.22	0.659	0.44
Without optimization	9.4814	9.4885	19.21	12.07	0.196	0.121
MLE strategy	9.4830	9.5091	16.86	8.83	0.179	0.096
APAM strategy	9.4950	9.4961	5.15	4.16	0.053	0.041

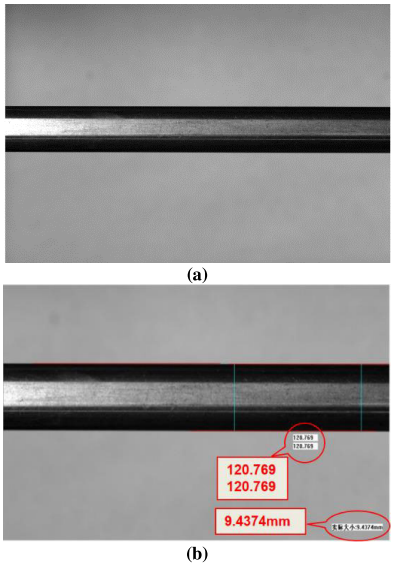

(a)

(b)

FIGURE 7. (a) Fuel rod to be measured with a diameter of 9.5 mm. The middle part of the fuel rod is caused by the reflection of light between the surface and the light source during shooting. (b) One of the results of fuel rod measurement.

the proposed optimization algorithm can be used to select a suitable measurement scheme.

The proposed method will have some influence on the optimization results in the selection of parameters such as learning factor, mutation rate, average particle distance and its minimum limit threshold, measuring whether the global optimal adaptation value changes significantly, and the number of particles. But these effects are much smaller than those caused by the PSO algorithm. Since the entire measurement process is operated remotely, certain irregular manual operations will also affect the measurement accuracy during the measurement process.

V. EXPERIMENTAL RESULTS

The diameter of the fuel rod is measured under the same experimental conditions of the above-mentioned cases. Different types of treatment are performed on the fuel rods to obtain corresponding diameters. Fig. 7 shows the fuel rod to be measured and one of the results of fuel rod measurement. And Table 14 has listed the relevant measurement errors of the two optimization methods.

Table 15 shows a numerical comparison of errors between measurement results of different types of treatment. Among the methods, the type ''without any treatments on image'' has scarcely high accuracy for a measurement device. However, these error data reflect the importance of distortion correction. Furthermore, MLE and APAM optimization strategies have a good effect on the correction of different positions of the fuel rod, especially the middle position. The results reveal that the APAM optimization strategy is superior.

VI. CONCLUSIONS

Accurate measurement of the diameter of nuclear fuel rods is of great significance to the safe and stable operation of nuclear power plants. This paper proposes an image processing-based APAM scheme for fuel rod diameter measurement. This scheme combines Zhang's camera calibration technique and takes second-order tangential distortion into consideration. And the camera is further corrected by the proposed camera parameter optimization method APAM. The obtained experimental results show that the relative error of is 0.041% and RMSE is 4.16 μm of the proposed scheme APAM, which demonstrates that APAM satisfies the demand for accurate. The main advantage of the proposed scheme is its high precision, because parameters optimization are considered and different ROIs are selected to obtain pixel equivalents, the measurement errors caused by camera distortion and corners detection are reduced. Therefore, the proposed APAM in this paper has high potential for practical applications.

REFERENCES

[1] K.-T. Kim, "A study on the grid-to-rod fretting wear-induced fuel failure observed in the 16 × 16KOFA fuel," *Nucl. Eng. Design*, vol. 240, no. 4, pp. 756–762, Apr. 2010.
[2] K.-T. Kim, "The effect of fuel rod oxidation on PCMI-induced fuel failure," *J. Nucl. Mater.*, vol. 418, nos. 1–3, pp. 249–260, Nov. 2011.
[3] J. L. Singh, N. Kumawat, A. K. Sinha, S. Bhat, K. Jayarajan, and C. Dey, *Development of a Set-Up for the Detection of Failed Fuels in TAPS BWR Spent Fuels Storage Bay*. Vienna, Austria: IAEA, 2003, pp. 283–286.
[4] S. V. Pavlov, "Detection of failed fuel rods in the VVER and RBMK fuel assemblies and results of detection method adoption," *Atomnaya Energiya*, vol. 106, no. 2, pp. 84–88, 2009.

[5] Z. D. Thome, W. C. A. Pereira, J. C. Machado, J. M. Seixas, and W. Soares-Filho, "A system for nuclear fuel inspection based on ultrasonic pulse-echo technique," *IEEE Trans. Nucl. Sci.*, vol. 58, no. 5, pp. 2452–2458, Oct. 2011.
[6] C. Leuthrot, A. Brissaud, and J. P. Missud, "Relation ships between the characteristics of cladding defects and the activity of the primary coolant circuit, an aid for the management of leaking fuel assemblies in PWR," in *Proc. Int. Topical Meeting Light Water React. Fuel Perform.*, Avignon, France, Apr. 1991, pp. 21–24.
[7] R. Beraha, G. Beuken, G. Frejaville, C. Leuthrot, and Y. Musante, "Fuel survey in the light water reactors based on the activity of the fission products," *Nucl. Technol.*, vol. 49, no. 3, pp. 426–434, Aug. 1980.
[8] H. Knaob, R. Stark, and R. Sturm, "Sipping equipment for leak testing of fuel assemblies in VVER-440 reactor," *Kerntechnik*, vol. 56, no. 2, pp. 94–97, 1991.
[9] Z. Tang, Y.-S. Lin, K.-H. Lee, J.-N. Hwang, and J.-H. Chuang, "ESTHER: Joint camera self-calibration and automatic radial distortion correction from tracking of walking humans," *IEEE Access*, vol. 7, pp. 10754–10766, 2019.
[10] Z. Zhang, "A flexible new technique for camera calibration," *IEEE Trans. Pattern Anal. Mach. Intell.*, vol. 22, no. 11, pp. 1330–1334, Nov. 2000.
[11] R. Tsai, "A versatile camera calibration technique for high-accuracy 3D machine vision metrology using off-the-shelf TV cameras and lenses," *IEEE J. Robot. Autom.*, vol. 3, no. 4, pp. 323–344, Aug. 1987.
[12] M. Niu, K. Song, X. Wen, D. Zhang, and Y. Yan, "The line scan camera calibration based on space rings group," *IEEE Access*, vol. 6, pp. 23711–23721, 2018.
[13] X. Gong, Y. Lv, X. Xu, Z. Jiang, and Z. Sun, "High-precision calibration of omnidirectional camera using an iterative method," *IEEE Access*, vol. 7, pp. 152179–152186, 2019.
[14] J. Park, S.-C. Byun, and B.-U. Lee, "Lens distortion correction using ideal image coordinates," *IEEE Trans. Consum. Electron.*, vol. 55, no. 3, pp. 987–991, Aug. 2009.
[15] R. Hartley and S. B. Kang, "Parameter-free radial distortion correction with center of distortion estimation," *IEEE Trans. Pattern Anal. Mach. Intell.*, vol. 29, no. 8, pp. 1309–1321, Aug. 2007.
[16] S. Thirthala and M. Pollefeys, "Multi-view geometry of 1D radial cameras and its application to omnidirectional camera calibration," in *Proc. 10th IEEE Int. Conf. Comput. Vis. (ICCV)*, vol. 1, Oct. 2005, pp. 1539–1546.
[17] W. Liu, S. Wu, X. Wu, and H. Zhao, "Calibration method based on the image of the absolute quadratic curve," *IEEE Access*, vol. 7, pp. 29856–29868, 2019.
[18] S.-H. Lee, S.-K. Lee, and J.-S. Choi, "Correction of radial distortion using a planar checkerboard pattern and its image," *IEEE Trans. Consum. Electron.*, vol. 55, no. 1, pp. 27–33, Feb. 2009.
[19] L. J. Fogel, *Evolutionary Programming in Perspective: The Top-Down View*. Piscataway, NJ, USA: IEEE Press, 1994, pp. 135–146.
[20] D. E. Goldberg, *Genetic Algorithm in Search, Optimization, and Machine Learning*. Chicago, IL, USA: Addison-Wesley, 1989.
[21] R. Eberhart, P. Simpson, and R. Dobbins, *Computational Intelligence PC Tools*. Boston, MA, USA: Academic, 1996, pp. 611–616.
[22] R. Eberhart and J. Kennedy, "A new optimizer using particle swarm theory," in *Proc. MHS Proc. 6th Int. Symp. Micro Mach. Hum. Sci.*, Oct. 1995, pp. 39–43.
[23] J. Kennedy and R. Eberhart, "Particle swarm optimization," in *Proc. Neural Netw. IEEE Int. Conf.*, Perth, WA, Australia, Dec. 1995, pp. 1942–1948.
[24] H.-R. Li and Y.-L. Gao, "Particle swarm optimization algorithm with adaptive threshold mutation," in *Proc. Int. Conf. Comput. Intell. Secur.*, Dec. 2009, pp. 129–132.
[25] W. Faig, "Calibration of close-range photogrammetric systems: Mathematical formulation," *Photogramm. Eng. Remote Sens.*, vol. 41, no. 12, pp. 1479–1486, Dec. 1975.
[26] C. B. Duane, "Close-range camera calibration," *Photogramm. Eng.*, vol. 37, pp. 855–866, Dec. 2002.
[27] D. C. Brown, "Decentering distortion of lenes," *Photogramm. Eng. Remote Sens.*, vol. 34, no. 3, pp. 444–462, May 1966.
[28] J. Weng, P. Cohen, and M. Herniou, "Camera calibration with distortion models and accuracy evaluation," *IEEE Trans. Pattern Anal. Mach. Intell.*, vol. 14, no. 10, pp. 965–980, Oct. 1992.
[29] J. Weng, P. Cohen, and M. Herniou, "Calibration of stereo cameras using a non-linear distortion model (CCD sensory)," in *Proc. 10th Int. Conf. Pattern Recognit.*, Jun. 1990, pp. 246–253.
[30] O. Cheng, W. Guangzhi, Z. Quan, K. Wei, and D. Hui, "Evaluating harris method in camera calibration," in *Proc. IEEE Eng. Med. Biol. 27th Annu. Conf.*, Jan. 2005, pp. 6383–6386.
[31] J. Shawash and D. R. Selviah, "Real-time nonlinear parameter estimation using the levenberg–marquardt algorithm on field programmable gate arrays," *IEEE Trans. Ind. Electron.*, vol. 60, no. 1, pp. 170–176, Jan. 2013.
[32] L. Lecam, "Maximum likelihood: An introduction," *Int. Stat. Rev.*, vol. 58, pp. 153–171, Aug. 1990.
[33] T. S. Ferguson, "An inconsistent maximum likelihood estimate," *J. Amer. Stat. Assoc.*, vol. 77, no. 380, pp. 831–834, Dec. 1982.
[34] J. Aldrich, "R.A. Fisher and the making of maximum likelihood 1912–1922," *Stat. Sci.*, vol. 12, no. 3, pp. 162–176, Sep. 1997.
[35] J. More, *The Levenberg-Marquardt Algorithm: Implementation, and Theory in Numerical Analysis* (Lecture Notes in Mathematics), G. A. Watson, Ed. Springer-Verlag, 1977.
[36] M. Anantathanavit and M.-A. Munlin, "Radius particle swarm optimization," in *Proc. Int. Comput. Sci. Eng. Conf. (ICSEC)*, Sep. 2013, pp. 126–130.
[37] T. Hu and H. Wu, "Study of micro-vision calibration technique based on SIFT feature matching," in *Proc. Int. Conf. Comput. Comput. Technol. Agricult.*, Beijing, China, 2012, pp. 270–276.
[38] J. Shi and Tomasi, "Good features to track," in *Proc. IEEE Conf. Comput. Vis. Pattern Recognit. CVPR*, Jun. 1994, pp. 593–600.

RUIRUI JI received the B.S. degree in automation from Anhui Polytechnic University, China, in 2018. She is currently pursuing the M.S. degree with the College of Mechatronics and Control Engineering, Shenzhen University.

Her research interests include image processing, phase retrieval, computer vision, and visual inspection of nuclear components, including measurement of key parameters of the fuel rod for operational safety.

PENG CHEN received the B.S. degree in automation from the Nanchang Institute of Engineering, China, in 2017. He is currently pursuing the M.S. degree with Shenzhen University.

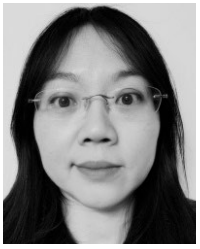

CHENGXIANG LIU received the M.S. degree in control theory and control engineering, in 2001, and the Ph.D. degree in navigation, guidance, and control from Harbin Engineering University, China, in 2003. She is currently a Professor with the College of Mechatronics and Control Engineering, Shenzhen University, China. Her research interests include digital image processing, new inertial device, and photoelectric sensors.

LI TU is currently a Professor with the Zhongshan Institute, University of Electronic Science and Technology of China. His research interests include chaos theory and applications, and algorithm research and analysis.

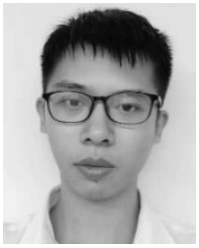

FULIN LIANG was born in Guangdong, China, in 1996. He received the B.S. degree from Shenzhen University, Shenzhen, China, in 2019, where he is currently pursuing the M.S. degree.

During the graduate student period, he mainly studies the image distortion correction and precision measurement of underwater images.

PANSHENG GU received the B.S. degree in automation from Shenzhen University, China, in 2019, where he is currently pursuing the M.S. degree.

CHEN HUANG received the B.S. degree in automation from Shenzhen University, China, in 2019, where he is currently pursuing the M.S. degree.

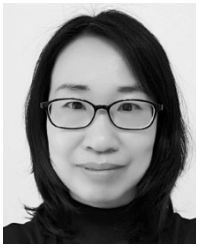

RONG YANG received the M.Phil. degree in electronic and electrical engineering from The Hong Kong University of Science and Technology, in 2000, and the Ph.D. degree in computer science from The Chinese University of Hong Kong, in 2005. She is currently an Associate Professor with the College of Mechatronics and Control Engineering, Shenzhen University, China. Her research interests include fuzzy theory, nonlinear integrals, nonlinear optimization, pattern recognition, soft computing techniques, and data mining.